Origin of Enantioreversal in the Rhodium-Catalyzed Asymmetric Hydrogenation of Prochiral Enamides and the Effect of the α-Substituent

Steven Feldgus and Clark R. Landis*

Department of Chemistry, University of Wisconsin−Madison, 1101 University Avenue, Madison, Wisconsin 53705

Received January 25, 2001

The enantioselectivity of prochiral enamide hydrogenation depends on the structure of the enamide, with particular sensitivity to the nature of the α-substituent. Recently, Burk has reported a spectacular example of structure sensitivity for [Rh(DuPHOS)]$^+$-catalyzed enamide hydrogenations: although enamides containing either carboxyl or *tert*-butyl α-substituents hydrogenate to ≥99% enantiomeric excess, the sense of enantioselection for the two substrate classes is reversed. Why should the magnitude and sense of enantioselectivity depend so strongly on the enamide α-substituent? We report the application of QM/MM (ONIOM) computations to address this long-standing issue in asymmetric catalysis. Specifically, we demonstrate that computational methods reproduce the α-substituent effect in enamide hydrogenation catalysis and probe how the interaction of the enamide C═C bond and the catalyst varies with the structure of the substrate. The picture that emerges emphasizes the complex confluence of both electronic effects (i.e., those effects that do not depend on the size of the model system) and steric effects in controlling the stereochemistry of enamide hydrogenation reactions.

Introduction

Enantioselective organotransition metal catalysts have revolutionized asymmetric synthesis. Beginning with the development of highly enantioselective catalysts for the hydrogenation of dehydroamino acids in the early 1970s,[1−3] there have been remarkable advances in the creation of new catalysts for a wide variety of chemical transformations. Enantioselective catalytic hydrogenations, epoxidations, isomerizations, polymerizations, and dihydroxylations now constitute a powerful set of methods for the efficient synthesis of natural and unnatural chiral materials.[4−7] Not surprisingly, such catalysts have had significant commercial impact.[8] Equally impressive are the rates and enantioselectivities exhibited by these modern organotransition metal complexes, some of which now rival the performance of highly efficient enzymes.[9−14]

A sample asymmetric catalytic hydrogenation is shown in Scheme 1. Early work with aryl diphosphine ligands (DIPAMP, etc.) demonstrated the need for an electron-withdrawing group on the α-carbon in order to obtain high enantioselectivities.[3,5,15] Knowles et al. found that the enantiomeric excess (ee) dropped from over 89% (R_α = methyl ester, carboxylic acid, or nitrile) to 51% when R_α = methyl. Koenig et al. used [Rh(DIPAMP)]$^+$ to hydrogenate a series of para-substituted 1-phenyl(acetyloxy)ethenes and observed a reduction in ee with decreasing electron-withdrawing ability of the para substituent (from 65% with NO_2 to 51% with OCH_3).[15] For both these studies, all hydrogenated products showed the same sense of chirality (*S* configuration with (*R*,*R*)-DIPAMP).

Early work with bis(phospholane) ligands concentrated on substrates with electron-withdrawing groups in the α-position. Very high enantioselectivities (>95%) were obtained through [Rh(DuPHOS)]$^+$-catalyzed hydrogenations of substrates with various ester, carboxylic acid, and aryl substituents on the α-carbon.[10,11] In all cases, the chirality of the product was the same as the chirality of the bis(phospholane) ligand (i.e., (*S*,*S*)-Me-DuPHOS leads to *S* product). Recently, Burk and coworkers reported the first highly enantioselective hydrogenation of a substrate with an alkyl group on the α-carbon.[16] With *t*-Bu as the α-substituent, >99% ee is obtained, but with the *opposite* sense of chirality (i.e.,

(1) Dang, T. P.; Kagan, H. B. *J. Am. Chem. Soc.* **1972**, *94*, 6429−6433.
(2) Fryzuk, M. D.; Bosnich, B. *J. Am. Chem. Soc.* **1977**, *99*, 6262−6267.
(3) Vineyard, B. D.; Knowles, W. S.; Sabacky, M. J.; Bachman, G. L.; Weinkauff, D. J. *J. Am. Chem. Soc.* **1977**, *99*, 5946−5952.
(4) Knowles, W. S. *Acc. Chem. Res.* **1983**, *16*, 106−112.
(5) Koenig, K. E. In *Asymmetric Synthesis*; Morrison, J. D., Ed.; Academic: Orlando, 1985; Vol. 5, pp 71−101.
(6) Ojima, I. *Catalytic Asymmetric Synthesis*; VCH: New York, 1993.
(7) Bosnich, B. In *Encyclopedia of Inorganic Chemistry*; King, R. B., Ed.; John Wiley & Sons: Chichester, 1994; Vol. 1, pp 219−236.
(8) Stinson, S. C. *Chem. Eng. News* **1999**, *77* (41), 101−120.
(9) Burk, M. J. *J. Am. Chem. Soc.* **1991**, *113*, 8518−8519.
(10) Burk, M. J.; Feaster, J. E.; Nugent, W. A.; Harlow, R. L. *J. Am. Chem. Soc.* **1993**, *115*, 10125−10138.
(11) Burk, M. J. *Chemtracts-Org. Chem.* **1998**, *11*, 787−802.
(12) Jiang, Q.; Jiang, Y.; Xiao, D.; Cao, P.; Zhang, X. *Angew. Chem., Int. Ed.* **1998**, *37*, 1100−1103.
(13) Jiang, Q.; Xiao, D.; Cao, P.; Zhang, X. *Angew. Chem., Int. Ed.* **1999**, *38*, 516−518.
(14) Zhang, Z.; Zhu, G.; Jiang, Q.; Xiao, D.; Zhang, X. *J. Org. Chem.* **1999**, *64*, 1774−1775.
(15) Koenig, K. E.; Bachman, G. L.; Vineyard, B. D. *J. Org. Chem.* **1980**, *45*, 2362−2365.

10.1021/om010060t CCC: $20.00
Publication on Web 05/03/2001

Scheme 1

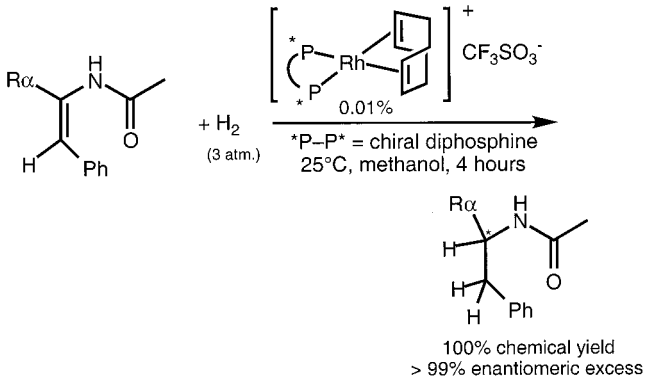

(*S*,*S*)-Me-DuPHOS yields *R* product) and a much slower rate. An identical reversal in product chiralty was observed by Gridnev et al. with their [(1,2-bis(*tert*-butylmethylphosphino)ethane)Rh]$^+$ catalyst.[17] These results dramatically demonstrate the critical effect of the α-substituent on the enantioselectivities, rates, and absolute configurations of rhodium-catalyzed asymmetric hydrogenation.

We previously have conducted several computational studies aimed at understanding the detailed mechanism of rhodium-catalyzed asymmetric hydrogenation.[18−20] Our work involved the addition of a model substrate, **1**, to the catalyst [((*R*,*R*)-Me-DuPHOS)Rh]$^+$ (Figure 1), which initially results in the formation of two diastereomeric catalyst−substrate adducts, **MAJ** and **MIN** (Figure 2).

Experimentally and computationally, the rate of reaction with H_2 is much faster for the less stable diastereomer, **MIN**. This "anti-lock-and-key" behavior arises from both electronic and steric factors. The greater stability of **MAJ** arises from the electronic preference for the enamide α-carbon to lie in the rhodium−diphosphine plane, which cannot occur in **MIN** due to steric hindrance from a DuPHOS methyl group. The reactivity of the diastereomers was examined by following the addition of H_2 along eight diastereomeric pathways (Figure 3). Addition of dihydrogen along the P−Rh−O axis (pathways **B** and **D**) generates large electronic barriers due to extensive nuclear reorganization.[18−20] Along the P−Rh−C axis, addition may either occur on the side of the α-carbon which leads to a *β*-alkyl hydride (pathway **C**) or on the side of the *β*-carbon which leads to an α-alkyl hydride (pathway **A**). Scheme 2 shows simplified α- and *β*-alkyl hydrides. Transition metal−alkyl *σ*-bonds are stronger when electron-withdrawing groups are placed on the carbon.[21] When R_α = CN, as in **1**, our computational studies found α-alkyl hydrides to be ∼10 kcal/mol more stable than *β*-alkyl hydrides. These thermodynamic distinctions also

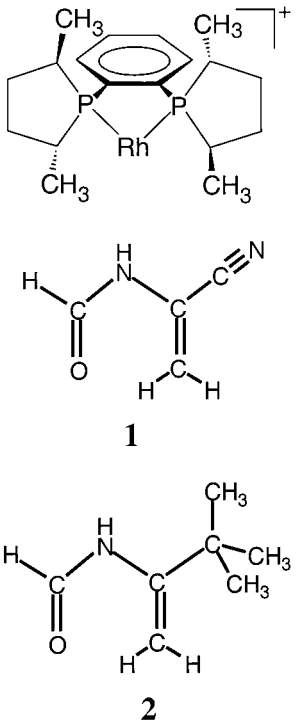

Figure 1. Catalyst and model enamide α-formamidoacrylonitrile, **1**, used in previous work.

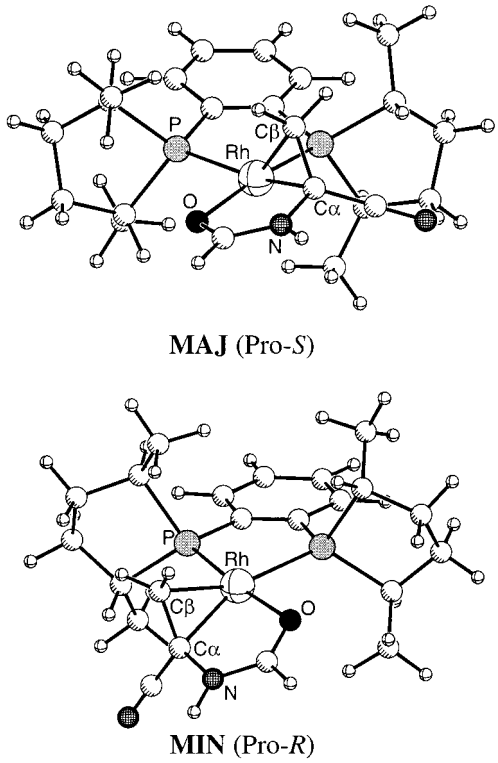

Figure 2. Optimized structures of both catalyst−enamide diastereomers at the ONIOM(B3LYP/LANL2DZ:HF/LANL2MB:UFF) level of theory. Pro-*R* and Pro-*S* indicate the enantiomer formed from each diastereomer upon hydrogenation.

are reflected in the insertion kinetic barriers to form α- and *β*-alkyl hydrides. Consequently, pathway **C** has a higher overall reaction barrier than **A** for both the major and minor manifolds. Addition along pathway **A** is hindered on the major manifold by steric repulsion

(16) Burk, M. J.; Casy, G.; Johnson, N. B. *J. Org. Chem.* **1998**, *63*, 6084−6085.
(17) Gridnev, I. D.; Higashi, N.; Imamoto, T. *J. Am. Chem. Soc.* **2000**, *122*, 10486-10487.
(18) Landis, C. R.; Hilfenhaus, P.; Feldgus, S. *J. Am. Chem. Soc.* **1999**, *121*, 8741−8754.
(19) Landis, C. R.; Feldgus, S. *Angew. Chem., Int. Ed.* **2000**, *39*, 2863−2866.
(20) Feldgus, S.; Landis, C. R. *J. Am. Chem. Soc.* **2000**, *122*, 12714−12727.
(21) Collman, J. P.; Hegedus, L. S.; Norton, J. R.; Finke, R. G. *Principles and Applications of Organotransition Metal Chemistry*; University Science Books: Mill Valley, 1987.

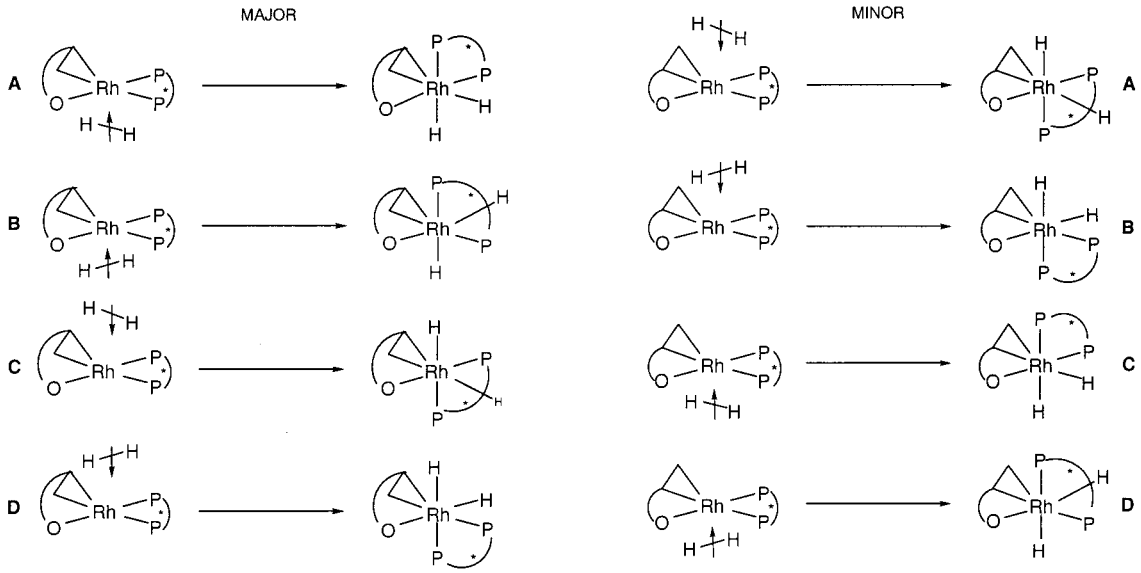

Figure 3. Eight possible isomeric pathways for addition of H_2 to the two catalyst−enamide adducts.

Scheme 2

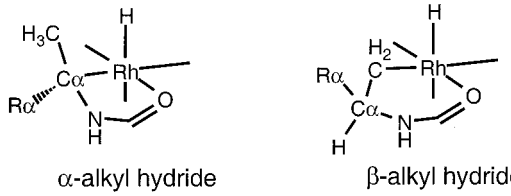

between the nitrile and DuPHOS methyl groups, making **MIN** the more reactive diastereomer.

Pathways **B** and **D** exhibit high barriers early in the reaction with H_2. These barriers are independent of the nature of the α-substituent and whether the diphosphine is chiral or achiral. As a result, pathways **B** and **D** are unlikely to be important in the hydrogenation of chelating enamide substrates.

On the basis of our prior computational results, it is natural to focus on pathway **C** as we seek a general explanation for the dramatic influence of the α-substituent on enantioselectivity. We expect the relative barriers to insertion along pathways **C** and **A**, as well as the relative stabilities of α- and *β*-alkyl hydrides, to be sensitive to the identity of the α-substituent. Pathway **C**, therefore, could become the reactive pathway if the α-alkyl hydride were sufficiently destabilized by, for example, the addition of a bulky electron-donating α-substituent. Pathway **C** is relatively free of steric hindrance on the major manifold, similar to pathway **A** on the minor manifold. Thus, our previous computational results hint at a possible explanation for the experimentally observed reversal in enantioselectivity when an electron-withdrawing functionality is replaced by a bulky, electron-donating α-substituent.

We report calculated reaction pathways for the [((*R*,*R*)-MeDuPHOS)Rh]$^+$-catalyzed hydrogenation of the *tert*-butyl-substituted enamide, *N*-(1-*tert*-butylvinyl)formamide (**2**), using the ONIOM hybrid method. The goals of these computations are to test the accuracy of modern computational methods in reproducing fine details of complex catalytic phenomena and to develop a more fundamental understanding of the α-substituent effect in enantioselective hydrogenations of prochiral enamides. In addition, we report the results of a series of computational experiments which are designed to explore how catalyst−enamide bonding and geometry respond to changes in the enamide α-substituent.

Computational Methods

ONIOM Calculations. The potential energy surface for hydrogenation of **2** was computed using Morokuma's ONIOM method[22,23] as implemented in Gaussian98.[24] Minor additions and corrections to the Gaussian98 molecular mechanics routines were necessary to enable calculations on this system; those additions are available as Supplementary Information.

The three geometry layers of the ONIOM calculation are shown in Figure 4. The core contains the reactive part of the catalyst system: the model enamide with *t*-Bu replaced by methyl to reduce computational time, an ethylene-bridged diphosphine ligand (with hydrogens replacing the phospholane rings), rhodium, and the dihydrogen molecule (not shown in Figure 4). For this layer we use density functional theory (DFT), with Becke's three-parameter hybrid functional (B3),[25] and Lee, Yang, and Parr correlation energies (LYP).[26] The B3LYP method has shown comparable accuracy to sophisticated post-Hartree−Fock (HF) methods in transition metal studies.[27,28] The intermediate layer includes the phospholane rings, without the methyl groups, plus the remainder of the

(22) Maseras, F.; Morokuma, K. *J. Comput. Chem.* **1995**, *16*, 1170−1179.
(23) Svensson, M.; Humbel, S.; Froese, R. D. J.; Matsubara, T.; Sieber, S.; Morokuma, K. *J. Phys. Chem.* **1996**, *100*, 19357−19363.
(24) Frisch, M. J.; Trucks, G. W.; Schlegel, H. B.; Scuseria, G. E.; Robb, M. A.; Cheeseman, J. R.; Zakrzewski, V. G.; Montgomery, J., J. A.; Stratmann, R. E.; Burant, J. C.; Dapprich, S.; Millam, J. M.; Daniels, A. D.; Kudin, K. N.; Strain, M. C.; Farkas, O.; Tomasi, J.; Barone, V.; Cossi, M.; Cammi, R.; Mennucci, B.; Pomelli, C.; Adamo, C.; Clifford, S.; Ochterski, J.; Petersson, G. A.; Ayala, P. Y.; Cui, Q.; Morokuma, K.; Malick, D. K.; Rabuck, A. D.; Raghavachari, K.; Foresman, J. B.; Cioslowski, J.; Ortiz, J. V.; Stefanov, B. B.; Liu, G.; Liashenko, A.; Piskorz, P.; Komaromi, I.; Gomperts, R.; Martin, R. L.; Fox, D. J.; Keith, T.; Al-Laham, M. A.; Peng, C. Y.; Nanayakkara, A.; Gonzalez, C.; Challacombe, M.; Gill, P. M. W.; Johnson, B.; Chen, W.; Wong, M. W.; Andres, J. L.; Gonzalez, C.; Head-Gordon, M.; Replogle, E. S.; Pople, J. A. *Gaussian 98*, revision A.6; Gaussian, Inc.: Pittsburgh, PA, 1998.
(25) Becke, A. D. *Phys. Rev. A* **1988**, *38*, 3098−3100.
(26) Lee, C.; Yang, W.; Parr, R. G. *Phys. Rev. B* **1988**, *37*, 785−789.
(27) Koch, W.; Hertwig, R. H. In *Encyclopedia of Computational Chemistry*; Schleyer, P. v. R., Ed.; John Wiley & Sons: Chichester, 1998; Vol. 2, pp 689−700.
(28) Brown, J. M.; Hofmann, P. *Organometallic Bonding and Reactivity: Fundamental Studies*; Springer-Verlag: Berlin, 1999.

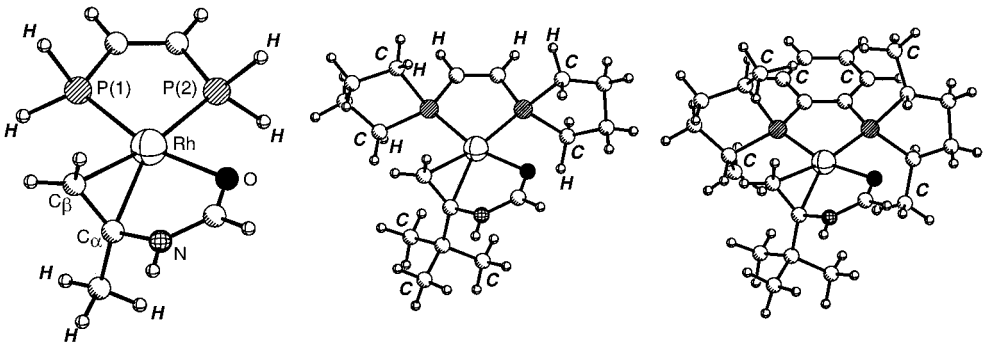

Figure 4. The three different layers of the ONIOM calculation. Link atoms are bold and italicized.

t-Bu group, and is treated with HF theory. The outer layer consists of the entire system and is modeled with the Universal Force Field (UFF) molecular mechanics method.[29] Any modifications to the enamide, such as in the experiments with different α-substituents, took place entirely within the core layer.

Most structures were initially found using a lower level ONIOM partitioning scheme that placed the *t*-Bu group in the MM layer, not the HF layer. This particular partition created intractable difficulties when attempting to perform calculations using larger basis sets. Moving *t*-Bu to the HF layer fixed this problem. Only reductive elimination transition states and hydrogenated product complexes were not reoptimized with the better ONIOM partitioning.

Geometry Optimization and Energies. ONIOM calculations are denoted by (High:Medium:Low), where High is the level of theory on the core, Medium is the level on the intermediate system, and Low is the level on the large system. All structures were initially optimized using (B3LYP/LANL2DZ:HF/LANL2MB:UFF), where LANL2DZ is the double-ζ quality Hay and Wadt basis set for the valence and penultimate shells, with effective core potentials (ECPs) at rhodium[30] and phosphorus,[31] and a Dunning/Huzinaga full double-ζ basis on C, H, N, and O.[32] LANL2MB is the same collection of effective core potentials, but with the minimal STO-3G basis[33] on C, H, N, and O, and a minimal basis set on the valence and penultimate shells of rhodium and phosphorus. This level of theory will be referred to as Basis I throughout this paper. For all *t*-Bu structures, geometry reoptimizations were performed using more sophisticated basis sets and effective core potentials from the Stuttgart group. The ECPs replaced 28 core electrons on rhodium and 10 on phosphorus. The Stuttgart valence basis sets used the following contraction schemes: (311111/22111/411) for rhodium[34] and (31/31) for phosphorus.[35] One d function with an exponent of 0.34 was added to phosphorus.[36] All other atoms used the 6-31G(d,p) basis set.[37−40] This level of theory, written in ONIOM notation as (B3LYP/Stuttgart:HF/LANL2MB:UFF), will be referred to as Basis II throughout this paper. As in our previous work, we found that the energies of certain intermediates and transition states were significantly lowered when a Basis II single-point energy was calculated for a Basis I geometry (Basis II//Basis I). Reoptimizing with Basis II (Basis II//Basis II) resulted in very small geometric and energetic changes. Most reported intermediates were verified as true minima by the absence of negative eigenvalues in the vibrational frequency analysis. Transition-state structures (indicated by ‡) were located using the synchronous-guided quasi-Newton method (STQN) until the Hessian matrix had only one imaginary eigenvalue.

For a number of transition states and intermediates, we were forced to apply geometric constraints. In those cases, we fixed the relevant geometric parameters to be equal to those from similar, fully optimized, structures. The energies obtained for these transition states are therefore upper bounds to the true transition state energies, and these are noted throughout the paper. Frequency analysis of the constrained jobs showed the proper number of negative frequencies in most cases: zero for intermediates and one for transition states. The residual forces on these structures, computed during the frequency analysis, are available in the Supporting Information.

Approximate free energies were obtained through thermochemical analysis of the frequency calculation, using the thermal correction to the Gibbs free energy as reported by Gaussian98. This takes into account zero-point effects, thermal enthalpy corrections, and entropy. All free energies reported in this paper are computed at 298 K, using unscaled frequencies.

NBO and CDA Analyses. We performed natural bond orbital (NBO) analysis[41] and charge decomposition analysis (CDA)[42] on all catalyst−enamide complexes. Unless otherwise noted, all these structures were fully optimized, with no constraints, in both the Pro-*R* and Pro-*S* binding configurations. To minimize computational time, NBO and CDA were performed on most molecules by replacing the DuPHOS ligand with a pair of PH_3 ligands at fixed geometry.

Results

Catalytic Hydrogenation of 2. Structures of Catalyst−Substrate Adducts. The optimized geometries of the diastereomeric catalyst−enamide adducts of [((*R*,*R*)-Me-DuPHOS)Rh]$^+$ **2**, **Pro-*R*** and **Pro-*S***, exhibit substantial differences from those of **1**. For ease of viewing, these geometries are depicted with the ligand represented as shaded quadrants (Figure 5). The dark quadrants represent the sterically encumbered regions

(29) Rappé, A. K.; Casewit, C. J.; Colwell, K. S.; Goddard, W. A., III; Skiff, W. M. *J. Am. Chem. Soc.* **1992**, *114*, 10024−10035.
(30) Hay, P. J.; Wadt, W. R. *J. Chem. Phys.* **1985**, *82*, 299−310.
(31) Hay, P. J.; Wadt, W. R. *J. Chem. Phys.* **1985**, *82*, 285−298.
(32) Dunning, T. H.; Hay, P. J. In *Modern Theoretical Chemistry*; Schaefer, H. F., Ed.; Plenum: New York, 1976; Vol. 3, p 1.
(33) Hehre, W. J.; Stewart, R. F.; Pople, J. A. *J. Chem. Phys.* **1969**, *51*, 2657−2664.
(34) Andrae, D.; Haeussermann, U.; Dolg, M.; Stoll, H.; Preuss, H. *Theor. Chim. Acta* **1990**, *77*, 123−141.
(35) Bergner, A.; Dolg, M.; Kuenchle, W.; Stoll, H.; Preuss, H. *Mol. Phys.* **1993**, *80*, 1431−1441.
(36) Huzinaga, S. *Gaussian Basis Sets for Molecular Calculations*; Elsevier: Amsterdam, 1984.
(37) Ditchfield, R.; Hehre, W. J.; Pople, J. A. *J. Chem. Phys.* **1971**, *54*, 724−728.
(38) Hehre, W. J.; Ditchfield, R.; Pople, J. A. *J. Chem. Phys.* **1972**, *56*, 2257−2261.
(39) Hariharan, P. C.; Pople, J. A. *Theor. Chim. Acta* **1973**, *28*, 213−222.
(40) Hariharan, P. C.; Pople, J. A. *Mol. Phys.* **1974**, *27*, 209−214.
(41) Reed, A. E.; Curtiss, L. A.; Weinhold, F. *Chem. Rev.* **1988**, *88*, 899−926.
(42) Dapprich, S.; Frenking, G. *J. Phys. Chem.* **1995**, *99*, 9352−9362.

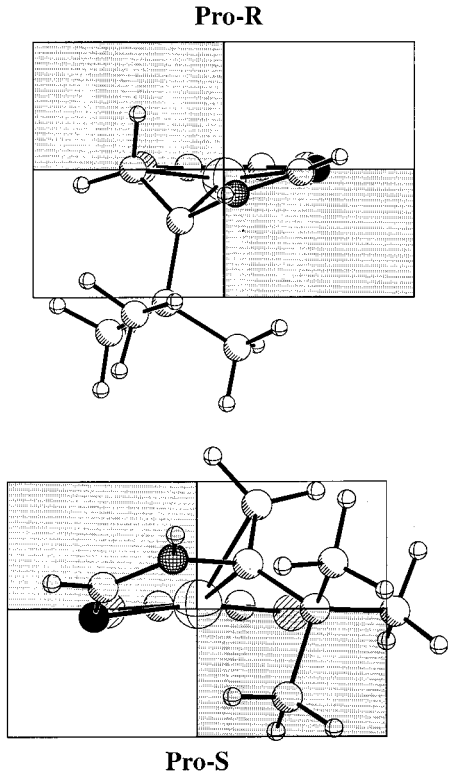

Figure 5. Structures of the two diastereomeric catalyst−enamide adducts, with the DuPHOS ligand rendered as a quadrant diagram.

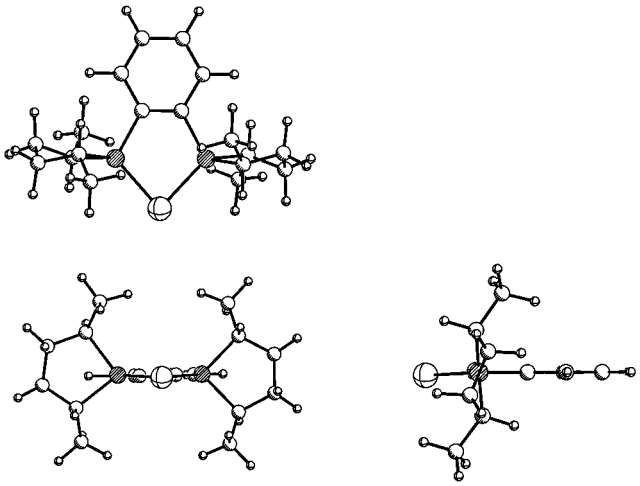

Figure 6. Lowest energy conformation of [(*R*,*R*)-Me-DuPHOS)Rh]$^+$. The ligand was allowed to fully optimize for each structure and remained largely unchanged.

occupied by the methyl groups of the (*R*,*R*)-Me-DuPHOS ligand, which is depicted in its lowest-energy conformation in Figure 6. The ONIOM energy of **Pro-*R*** is 0.46 kcal/mol lower than that of **Pro-*S***. Inclusion of free energy contributions makes the two diastereomers effectively identical in energy (**Pro-*R*** is more stable by 0.07 kcal/mol). We previously found for substrate **1** that the diastereomers **MIN** and **MAJ** (corresponding to **Pro-*R*** and **Pro-*S***, respectively[43]) are separated by ca. 4 kcal/mol in free energy. The structures depicted in Figure 5 clearly show the double bond avoiding the DuPHOS methyl groups in the hindered quadrants. For the **Pro-*R*** diastereomer, the C=C double bond lies nearly parallel to the P−Rh−P plane, whereas the C=C double bond of the **Pro-*S*** diastereomer is perpendicular but with its midpoint displaced 31° out of plane. More details of the geometries of these adducts and others are discussed in a later section.

Reaction with H_2. In our previous two computational studies, hydrogenation of α-formamidoacrylonitrile (**1**) with $[Rh(PH_3)_2]^+$ [18] and [Rh(Me-DuPHOS)]$^+$,[19,20] we followed all isomeric pathways (four for PH_3 and eight for Me-DuPHOS), as shown in Figure 3, through the following sequence of elementary steps:

1. Addition of hydrogen to give a weakly bound ion-induced dipole species (**SQPL** in the PH_3 study, **IID** in the DuPHOS study);
2. Further addition of hydrogen to give stable five-coordinate molecular hydrogen complexes (**MOLH$_2$**);
3. Oxidative addition of hydrogen to generate a six-coordinate, pseudo-octahedral dihydride complex (**DIHY**);
4. Migratory insertion of an olefin carbon into a Rh−H bond to form a five coordinate alkyl hydride (**ALHY**);
5. Reductive elimination of C−H from the alkyl hydride to produce the alkane product, still coordinated to the catalyst (**PROD**).

Starting from **Pro-*R*** and **Pro-*S*** (Figure 5), we followed the sequence of elementary steps listed above. Pathways **B** and **D** were not followed in this study because we previously found that kinetic barriers associated with formation of molecular H_2 complexes preclude any significant flux through these pathways. The potential energy surface for the reaction of **Pro-*R*** and **Pro-*S*** with H_2, up to the formation of alkyl hydrides, is shown in Figure 7. Intermediates and transition states are given the prefix ***R*-** or ***S*-** to denote whether they are on the **Pro-*R*** or **Pro-*S*** manifold. We further distinguish alkyl hydrides and their transition states with an α or ***β*** label, to indicate whether the Rh−C bond is between the α-carbon or the *β*-carbon. In some cases, geometric constraints were necessary to locate intermediates or transition states. The labels for these structures are italicized. Forces for the constrained structures, and details of the constraints, are available as Supporting Information.

In this study we neglect pathways that proceed via dissociation of the C=C double bond, as well as isomerization between different pathways. The tremendous dimensionality of isomerization and dissociation processes, and the potential effect of solvent on each, prohibits such analyses at this time. In our previous work we have explored isomerization among pathways A−D. There we concluded that most isomerization mechanisms are unlikely, but cannot rule out all possible mechanisms. Another possible set of pathways, which we have not included in our current investigations and which have found experimental support in the beautiful studies of Gridnev and Imamoto, involve H_2 oxidative addition prior to binding of the substrate.[44] Computational probes of such pathways are in progress. Transition states leading from *trans*-alkyl hydrides to *cis*-alkyl hydrides were not found due to computational time limitations. However, by analogy to our previous work,

(43) MAJOR and MINOR refer to diastereomer stabilities in α-formamidoacrylonitrile. The stabilities are reversed in this work, making these labels inappropriate.

(44) Gridnev, I. D.; Higashi, N.; Asakura, K.; Imamoto, T. *J. Am. Chem. Soc.* **2000**, *122*, 7183−7194.

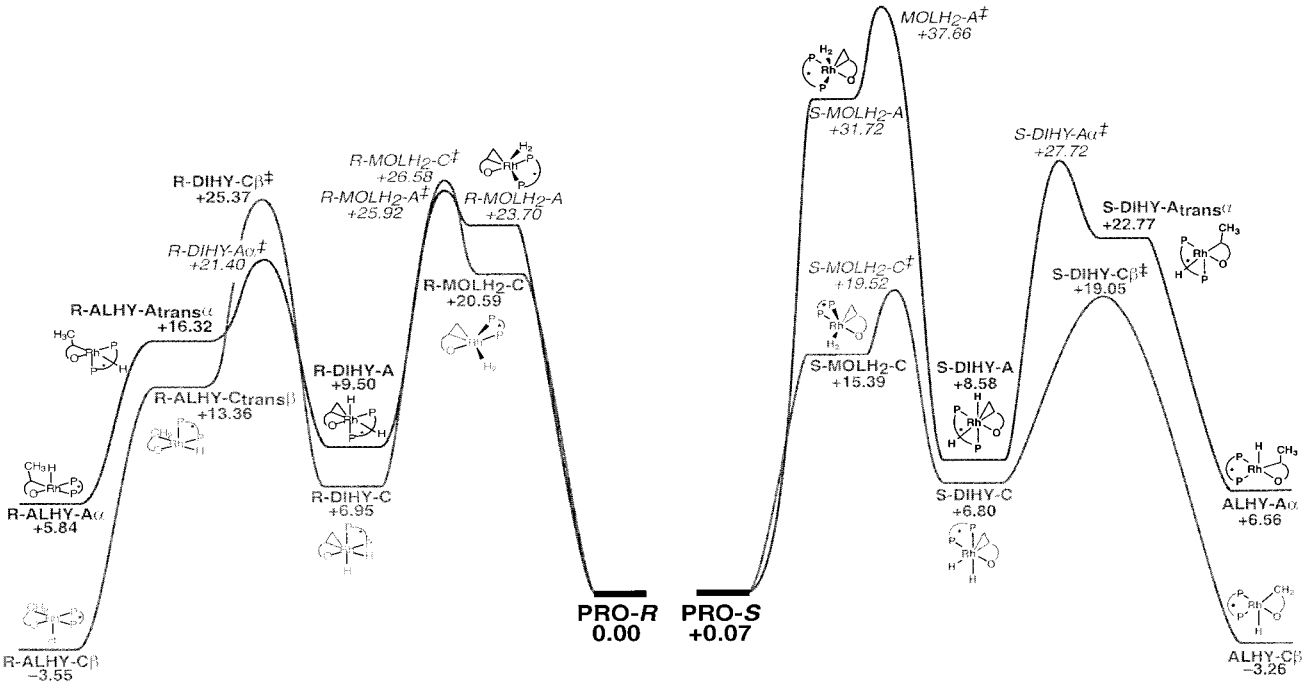

Figure 7. Free energy (kcal/mol) surface for the reaction of **Pro-*R*** and **Pro-*S*** with H_2. Constrained structures are labeled in italics.

we expect the barriers for this isomerization process to be small (ca. 1 kcal/mol) and, hence, not to affect the conclusions of this work.

Optimized geometries for all intermediates and transition states along the lowest energy pathways for **Pro-*R*** and **Pro-*S*** are presented in Figures 8 and 9 (similar figures for the two higher energy pathways are provided in the Supporting Information). The ONIOM energies, which do not include any entropic, zero-point, or thermal corrections, are listed for the structures from Figure 7 in Table 1. Reductive elimination transition states and coordinated alkane product complexes, which were calculated at a slightly different level of theory, are listed in Table 2. Critical attributes of the reaction pathway for the hydrogenation of **2** (Figure 7) differ from that of **1**. Most relevant for comparison with existing experimental data, the enantioselectivity for hydrogenation of **2** is computed to be high but of the sense opposite of that of **1**. Along the **Pro-*R*** pathways, the bulky *tert*-butyl substituent of **2** strongly destabilizes the association of H_2 due to clashing of the *tert*-butyl group with the methyl groups of the Me-DuPHOS ligands; the result is high (>20 kcal/mol) transition state free energies for H_2 association. The *tert*-butyl substituent does not strongly influence the addition of H_2 along the **Pro-*S*** pathway **C**, because addition of H_2 is coupled with small movement of the coordinated C=C double bond in an unhindered quadrant. These effects are depicted qualitatively using quadrant diagrams in Figure 10. As the reaction progresses from molecular dihydrogen complexes (**MOLH$_2$**) through oxidative addition to form dihydrides (**DIHY**), the *tert*-butyl substituent has little influence that is not already reflected in the relative energies of the molecular hydrogen complex isomers. It is in the migratory insertion of the alkene into the Rh−H bonds to form alkyl hydride complexes (**ALHY**) that the stereoelectronic influence of the *tert*-butyl group next affects enantioselection in catalytic hydrogenation. Relative to substrate **1**, the α-alkyl hydrides are strongly destabilized, thermodynamically, for substrate **2**. The formation of *β*-alkyl hydrides is exergonic, and the barrier to insertion along the **C** pathway of the **Pro-*S*** diastereomer is clearly the lowest of all the insertion barriers. Thus, to a good approximation, reversal of the sense of enantioselection can be traced to the destabilization of α-alkyl hydrides relative to the *β*-alkyl hydrides.

Destabilization of the α-alkyl hydrides clouds assignment of the turnover-limiting step for hydrogenation of **2**. For the hydrogenation of **1**, we previously identified oxidative addition of H_2 as turnover-limiting along both the **MAJ** and **MIN** manifolds. However, we note that the differences in computed free energies between oxidative addition and migratory insertion transition states were less that 3 kcal/mol. With **2** as the substrate, oxidative addition and migratory insertion transition states are even closer in energy, with differences of ca. 1 kcal/mol. Regardless of the turnover-limiting step, it is clear that the dominant alkyl hydride produced upon addition of H_2 to an equilibrating mixture of **Pro-*R*** and **Pro-*S*** will be the *β*-alkyl hydride **ALHY-C*β***. Reductive elimination barriers (see Table 2) are small (10−15 kcal/mol) and should not be rate determining, even at the low temperatures that have led to trapping of alkyl hydride intermediates in previous experimental studies.

The Nature of Catalyst−Enamide Binding and the Influence of α-Substituents. Diastereomer Stabilities. To test the electronic affect of the α-substituent on diastereomer stability, we examined three classes of enamide substrates: strongly electron withdrawing (R_α = CN and CO_2H), weakly electron donating (R_α = CH_3 and H), and strongly electron donating (R_α = *t*-Bu and NH_2). Two additional substrates, one with a nitrile on the *β*-carbon (***β*CN**) and one with R_α = H and the amide NH replaced by CH_2 (**3**), were used to

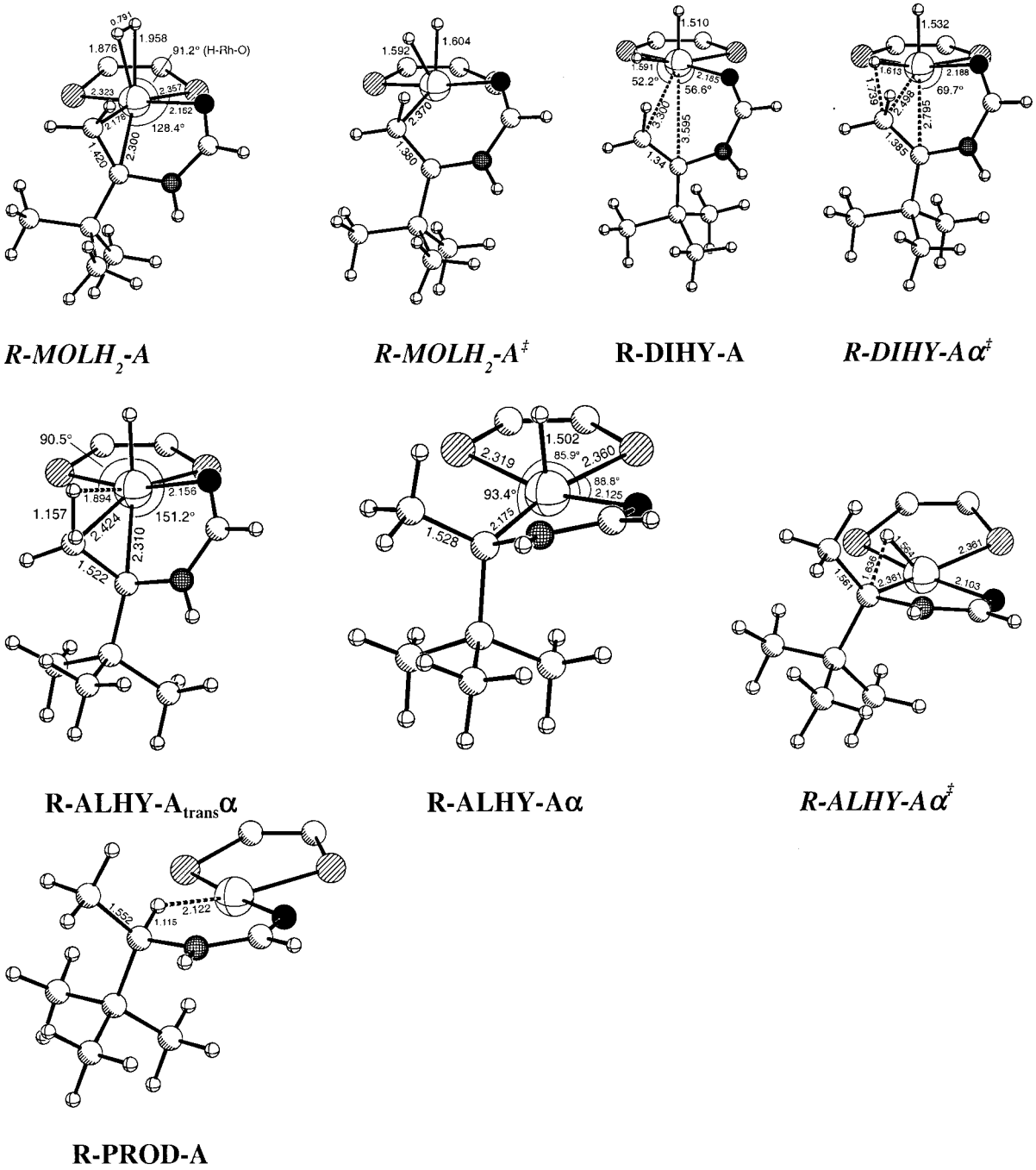

Figure 8. Optimized geometries for structures along pathway **A** of the **Pro-*R*** manifold. Constrained structures are italicized.

probe the influence of substituent position and chelate ring flexibilty, respectively, on diastereomer stabilities.

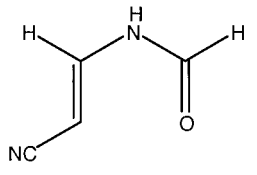

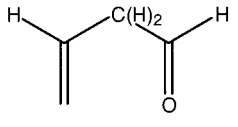

A consistent nomenclature for the diastereomeric catalyst−substrate adducts is difficult because binding of the same alkene face can result in different stereochemical designations depending on the priority of the substituents. We therefore use the nitrile-substituted enamide as our model and label the diastereomers *R*- and *S*- to indicate the enantiomer formed upon hydrogenation of each diastereomer as if it were a nitrile substituted in the α-position. Figure 11 shows the two different orientations of the enamide overlaid on a quadrant diagram[4] of [((*R*,*R*)-Me-DuPHOS)Rh]$^+$. The structures of all diastereomers were optimized with the *R*,*R*-Me-DuPHOS ligand and with an achiral version of the ligand for which the methyl groups of the Me-DuPHOS stereogenic centers were replaced with hydrogens. With the achiral diphosphine the resulting enantiomeric *R*- and *S*-structures had nearly identical energies (to within 0.5 kcal/mol, except for R_α = *tert*-butyl). However, the geometries could differ signifi-

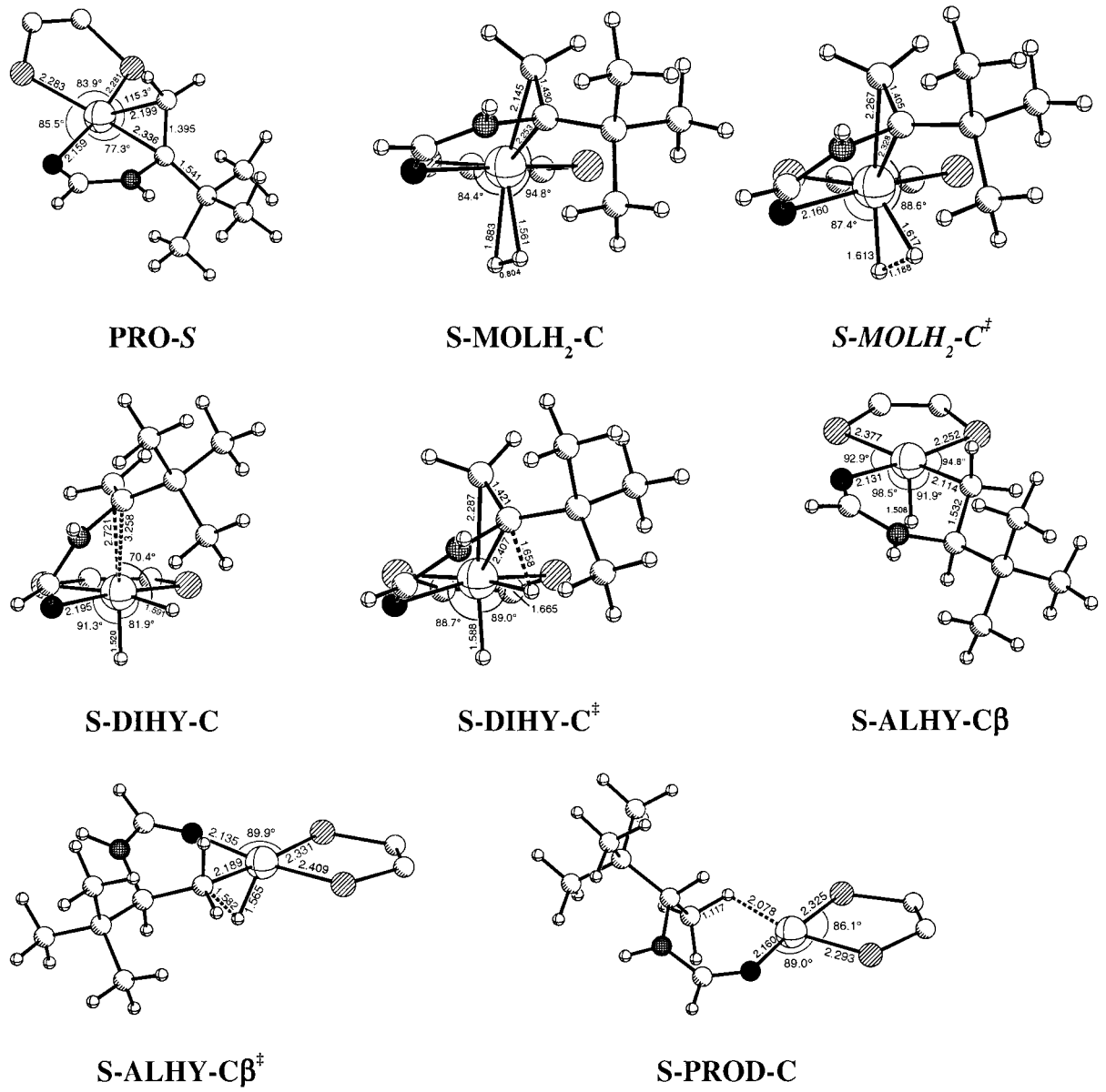

Figure 9. Optimized geometries of structures along pathway **C** of the **Pro-*S*** manifold. Constrained geometries are italicized.

Table 1. ONIOM Total Energies of All Intermediates and Transition States Found in This Study[a]

R-MOLH$_2$-A	11.18	**S-MOLH$_2$-A**	19.18
R-MOLH$_2$-C	8.09	**S-MOLH$_2$-C**	2.37
R-MOLH$_2$-A‡	15.08	**S-MOLH$_2$-A‡**	25.16
R-MOLH$_2$-C‡	17.70	**S-MOLH$_2$-C‡**	7.53
R-DIHY-A2	0.83	**S-DIHY-A2**	0.38
R-DIHY-C	−2.87	**S-DIHY-C**	−2.66
R-DIHY-Aα‡	9.47	**S-DIHY-Aα‡**	15.41
R-DIHY-C*β*‡	13.83	**S-DIHY-C*β*‡**	7.20
R-ALHY-A$_{trans}$α	1.29	**S-ALHY-A$_{trans}$α**	7.25
R-ALHY-C$_{trans}$*β*	0.24		
R-ALHY-Aα	−8.95	**S-ALHY-Aα**	−7.95
R-ALHY-C*β*	−15.48	**S-ALHY-C*β***	−15.53

[a] All energies are relative to **Pro-*R*** + H_2 at the Basis II/Basis II level.

cantly, indicating a very flat potential energy surface and a failure to reach the global minimum from both starting points.

The trends in diastereomer stabilities reveal that electron-withdrawing groups in the α-position enhance diastereoselectivity. As the α-substituent increases in electron-donating quality from $-CH_3$ to $-NH_2$, the sense of diastereoselection inverts. Placing the electron-withdrawing −CN in the *β*-position decreases the diastereoselectivity, and the substrate **3** yields little diastereoselectivity. Using the ONIOM partitioning, it is clear that the energetic trends are set by the relative energies of the QM core sections for the different catalyst−substrate adducts. This does *not* mean that steric effects are unimportant, however, as the MM shell has a dramatic effect on the structure, which in turn influences the energies. How the structures are affected by the α-substituents are discussed in the next section.

Structures of Diastereomeric Pairs. The parameters we use to monitor the changes in the structures of the diastereomeric catalyst−substrate adducts are shown in Figure 12. The rhodium diphosphine plane and C−C double bond are shown. The rise angle is positive if the midpoint of the C−C bond is "above" the plane (above as seen in Figure 3) and negative if the midpoint is "below" the plane. The pitch angle measures how much the double bond is leaning in toward rhodi-

Table 2. Approximate Free Energies (kcal/mol) of Alkyl Hydrides (ALHY), Reductive Elimination Transition States (ALHY‡), and Coordinated Hydrogenated Products (PROD) for Pathways A and C, at the Basis II/Basis I Level (frequencies at Basis I), Relative to H_2 + Pro-*S* at the Same Level of Theory[a]

pathway	ALHY	ALHY‡	red. elim. barrier	PROD
R−A	6.92 (−8.66)	21.27 (7.69)	14.35 (16.29)	−8.36 (−21.58)
R−C	−4.30 (−16.89)	5.77 (−5.70)	10.07 (11.17)	−10.54 (−22.72)
S−A	5.77 (−9.06)	20.31 (6.62)	14.54 (15.68)	−9.22 (−22.36)
S−C	−3.94 (−16.83)	6.29 (−5.52)	10.23 (11.31)	−7.69 (−20.56)

[a] Potential energies (without free energy contributions) are in parentheses.

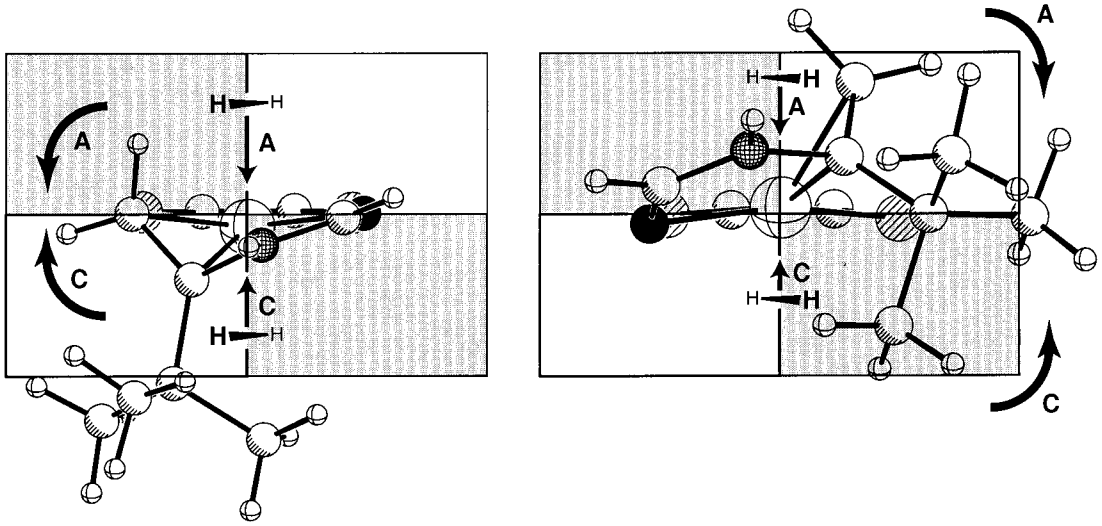

Figure 10. Addition of dihydrogen to the **Pro-*R*** (left diagram) and **Pro-*S*** (right) diastereomers, showing the direction of motion of the double bond upon addition via the **A** and **C** pathways. Pathway **C** for the **Pro-*S*** diastereomer has the smallest barrier to association of H_2 and pathway **A** for the same diastereomer has the highest.

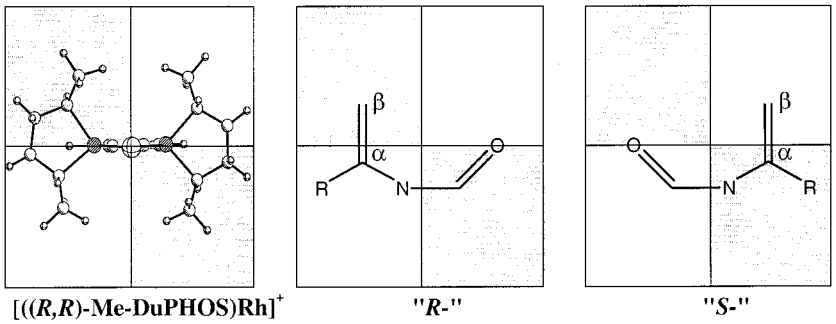

Figure 11. Nomenclature for each set of diastereomers. Regardless of the substituents, we refer to all structures as *R* or *S* if they are oriented as shown here.

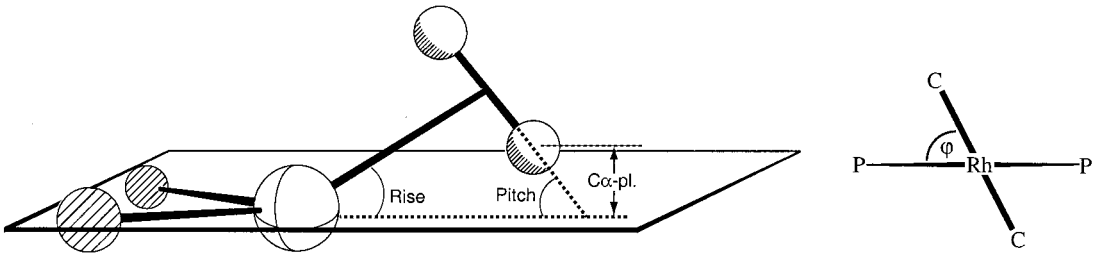

Figure 12. Illustration of geometric parameters used to compare structures.

um. The pitch angle and the distance of the carbons from the diphosphine plane along the C−C bond vector can be used to find the vertical distance of each carbon above or below the plane. The coplanarity angle, φ, measures the angle between the P−Rh−P and C−Rh−C planes. The vertical distances from each carbon to the Rh−diphosphine plane are labeled C_α−pl and C_β−pl.

The geometric data for the diastereomeric catalyst−substrate adducts are given in Table 4. First, we examine the "achiral" diphosphine complexes because these best represent the idealized structures in the absence of a chiral environment. This part of our examination addresses two questions: Are similar optimized structures obtained when starting from different diastereomers? Is there an intrinsic preference for the enamide C_α to lie in the P−Rh−P plane with the C═C bond perpendicular to the plane? With respect to the former question, although optimization with the

Table 3. Energies for the *R*-Diastereomer Relative to the *S*-Diastereomer for Chiral Structures, Broken Down into Difference by ONIOM Level[a]

$\Delta E = E(R) - E(S)$

R_α	ΔQM energy (kcal/mol) Δcore	Δintermed.	total ΔQM	ΔMM energy (kcal/mol)	Δtotal *E* (kcal/mol)
−CN	+1.60	+2.07	+3.67	+0.71	+4.38
$-CO_2H$	+3.42	+1.32	+4.74	+1.35	+6.09
$-CH_3$	+0.43	+0.42	+0.85	+0.06	+0.95
−H	+0.48	+0.29	+0.77	+0.62	+1.39
−*t*-Bu (Basis II)	−1.15	+0.09	−1.06	+0.60	−0.46
−*t*-Bu (achiral)	−0.53	−0.43	−0.96	−0.31	−1.27
$-NH_2$	−0.13	−0.75	−0.88	−0.90	−1.77
***β*CN**	+0.88	−0.30	+0.58	+0.43	+1.02
3	−0.09	−0.14	−0.23	+0.03	−0.20

[a] All diastereomers except for $R_\alpha = -t$-Bu, are optimized at the Basis I level. All energies of achiral structures other than $R_\alpha = -t$-Bu are identical to within 0.5 kcal/mol.

"achiral" diphosphine does not yield exactly the same structures and energies, most notably for the very bulky *t*-Bu substituent, it is clear that the pairs of "achiral" structures for all but the *t*-Bu case approach the same minimum. For the substrates with small and/or electron-withdrawing C_α substituents (i.e., R_α = −CN, −H, $-CH_3$), there is a clear preference for C_α to lie in the P−Rh−P plane with the C═C perpendicular. These preferences are indicated by short C_α-pl distances, longer C_β-pl distances, and coplanarity angles (φ) in the range of 65−85°. Accordingly, in all of these complexes the midpoint of the C═C bond lies substantially out of the P−Rh−P plane, yielding rise angles of ca. 25°. Interestingly, for $R_\alpha = -NH_2$, a substituent that is electron donating with respect to the alkene π-system, and **3**, the C═C bond centroid lies close to the P−Rh−P plane. For $R_\alpha = -NH_2$, C_β lies closer to the P−Rh−P plane than C_α. Although these systems are somewhat constrained by chelation, the data indicate that the electronic influence of the α-substituent strongly modulates the disposition of the alkene with respect to the idealized square plane. Apparently for $R_\alpha = -t$-Bu, the extreme bulkiness of the group leads to a very flat potential energy surface for large-scale motion of the C═C within the Rh coordination environment.

We now turn to the differentiation between *R* and *S* diastereomers in the presence of the full (*R*,*R*)-Me-DuPHOS ligand. Momentarily disregarding the *t*-Bu substituent, it is clear that the more stable diastereomer is always that whose structure more closely resembles the "achiral" structure. In other words, the steric interactions with the chiral diphosphine distort the less stable diastereomer away from its idealized geometry. For the strong electron-withdrawing −CN substituent, the idealized geometry places C_β well outside of the P−Rh−P plane. For the less stable diastereomer, this geometry places C_β deep in a hindered quadrant, and substantial distortion and energetic destabilization result. It is clear that the sense of diastereoselection is intimately connected to whether C_β or C_α prefers to lie in the coordination plane. This interpretation runs contrary to the common notion that it is the steric interaction of the α-substituent that controls diastereoselection in binding.

Bonding Analysis. At this point it is clear that the midpoint of the substrate C═C bond does not lie in the P−Rh−P carbon plane. Whether C_α or C_β lies in the plane depends on the nature of the α-substituent: π-electron-donating substituents such as $-NH_2$ favor C_β to lie in the coordination plane, while electron-withdrawing substituents such as −CN favor C_α to lie in that plane. To better understand the electronic origins of these structural motifs, we have analyzed the electronic structures of simple model systems using charge decomposition analysis (CDA)[42] of some catalyst−substrate adducts. To perform the CDA analysis, we modeled the adducts by taking the optimized geometries of diastereomers from Table 4 and replacing the DuPHOS ligand with two PH_3 groups fixed in the positions of the DuPHOS phosphorus atoms. Separate DFT computations were performed on the individual substrate and $[Rh(PH_3)]^+$ fragments. CDA decomposes the Rh−enamide bonding in terms of the Dewar−Chatt−Duncanson model of donation and back-donation.[45,46] The results are given in Table 5. The small residual terms, $q(s)$, indicate the bonding in these molecules can be properly considered as a donor−acceptor interaction. Back-donation decreases sharply as electron-donating groups are used, while donation stays fairly constant for all structures. The more stable diastereomer is that which maximizes metal-to-ligand back-bonding, with the very bulky R_α = *t*-Bu being the exception. The amount of back-bonding also correlates with the C−C bond lengths of Table 4, as expected. Similar results are found from natural bond orbital calculations, available in the Supporting Information.

Why is the centroid of the C═C bond so strongly displaced from the P−Rh−P coordination plane? While our work was in progress, Brown, Drew, and co-workers independently explored the same issue using both computations and empirical data.[47] For a broad selection of square-planar alkene complexes, they too found that electron-donating substituents shift the substituted C away from the coordination plane and electron-withdrawing substituents have the opposite effect. These authors note that the "alkene terminus which forms the better σ bond is shifted towards the square plane".[47] We briefly present both a canonical molecular orbital (MO) and a simple valence bond (VB) perspective on the nature of the Rh−enamide interaction.

Simplified canonical MOs for the catalyst and substrate fragments are shown in Figure 13. In accordance with the Dewar−Chatt−Duncanson model, bonding is dominated by donation of electron density from the filled alkene π-orbitals into the metal LUMO. For this interaction, the best match of donor and acceptor orbitals occurs with electron-donating α-substituents. Back-donation from metal lone pairs to the enamide can occur from any of three lone pairs. The stabilization energy will be maximized when back-donation occurs from the highest energy lone pair: d_{z^2}. As Scheme 3 shows, only double bonds that are significantly raised out of the plane can interact with d_{z^2}. The effect of the electron-withdrawing acceptor (A) reinforces the stabilization by lowering the energy of π^* and polarizing it toward C_β, which shortens the Rh−C_β bond length. The d_{z^2} orbital also mixes with other orbitals to point toward C_β and

(45) Dewar, J. M. S. *Bull. Soc. Chim. Fr.* **1951**, *18*, C71−C79.
(46) Chatt, J.; Duncanson, L. A. *J. Chem. Soc.* **1953**, 2939−2947.
(47) Price, D. W.; Drew, M. G. B.; Hii, K. K.; Brown, J. M. *Chem. Eur. J.* **2000**, *6*, 4587−4596.

Table 4. Computed Geometric Data for Diastereomeric Pairs Containing the Chiral *R,R*-MeDuPHOS Ligand and Its Demethylated, "Achiral" Form[a]

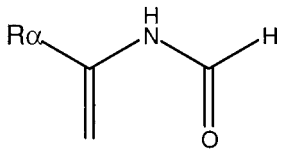

		distances (Å)					angles (deg)		
R_α		Rh−Cα	Rh−Cβ	Cα−Cβ	Cα−pl.	Cβ−pl.	rise	pitch	coplanarity
−CN	*R*-	2.169	2.228	1.421	1.01	0.39	−8.7	79.0	65.6
	S-	***2.192***	***2.136***	***1.440***	***0.54***	***1.69***	***+33.9***	***52.8***	***86.3***
−CN (achiral)		2.170	2.116	1.445	0.26	1.53	+26.3	61.4	82.8
		2.171	*2.101*	*1.452*	*0.54*	*1.70*	*+33.9*	*52.8*	*85.6*
$-CO_2H$		2.186	2.193	1.421	0.61	0.82	+2.9	87.4	64.3
		2.199	***2.093***	***1.450***	***0.57***	***1.70***	***+34.1***	***51.4***	***84.8***
$-CH_3$		2.194	2.233	1.412	0.25	1.12	−11.9	76.5	60.6
		2.209	***2.140***	***1.430***	***0.31***	***1.55***	***+27.2***	***59.9***	***82.6***
$-CH_3$ (achiral)		2.210	2.198	1.417	0.28	1.10	+11.2	78.1	73.7
		2.210	*2.195*	*1.417*	*0.32*	*1.55*	*+27.1*	*60.0*	*82.9*
−H		2.149	2.216	1.415	1.06	0.32	−10.4	76.8	70.7
		2.165	***2.135***	***1.432***	***0.37***	***1.60***	***+29.2***	***59.5***	***84.9***
−H (achiral)		2.167	2.171	1.420	0.13	1.24	+15.7	74.4	76.8
		2.165	*2.143*	*1.429*	*0.27*	*1.51*	*+27.2*	*59.9*	*82.9*
−*t*-Bu (Basis II)		**2.298**	**2.281**	**1.382**	**0.81**	**0.57**	**−3.1**	**87.6**	**39.9**
		2.336	*2.199*	*1.395*	*0.57*	*1.69*	*+31.4*	*52.7*	*69.9*
−*t*-Bu (achiral)		**2.265**	**2.264**	**1.385**	**0.72**	**0.66**	**−0.7**	**89.3**	**36.9**
		2.306	*2.207*	*1.393*	*0.35*	*1.55*	*+26.4*	*59.4*	*66.1*
$-NH_2$		**2.242**	**2.198**	**1.422**	**1.33**	**0.04**	**−17.9**	**74.0**	**66.4**
		2.403	*2.226*	*1.404*	*0.60*	*0.78*	*+2.3*	*80.0*	*62.9*
$-NH_2$ (achiral)		2.271	2.194	1.416	0.89	0.52	−5.0	88.2	69.3
		2.265	*2.195*	*1.418*	*1.01*	*0.39*	*−8.6*	*84.3*	*68.9*
***β*CN**		2.110	2.205	1.441	1.33	0.0	−19.0	67.0	71.8
		2.150	***2.136***	***1.448***	***0.27***	***1.55***	***+26.8***	***62.6***	***82.7***
***β*CN** (achiral)		*2.151*	*2.154*	*1.441*	*0.14*	*1.24*	*+15.8*	*74.3*	*77.6*
		2.152	*2.129*	*1.451*	*0.43*	*1.66*	*+31.3*	*57.7*	*83.4*
3 (achiral)		**2.212**	**2.193**	**1.411**	**0.39**	**1.00**	**+8.3**	**80.8**	**80.6**
		2.209	*2.200*	*1.410*	*0.56*	*0.85*	*+3.9*	*85.6*	*80.6*

[a]The *S* diastereomer data are italicized and the more stable diastereomer data are shown in bold. All structures except for $R_\alpha = -t$-Bu are optimized at Basis I.

Table 5. CDA Analysis for Selected Diastereomeric Structures[a]

R_α		donation (d)	back-donation (b)	d/b	*q*(*r*)	*q*(*s*)
−CN	*R*-	0.637	0.252	2.53	−0.426	−0.04
	S-	***0.636***	***0.279***	***2.28***	***−0.445***	***−0.02***
$-CO_2H$		0.639	0.234	2.73	−0.413	−0.04
		0.646	***0.256***	***2.52***	***−0.449***	***−0.02***
$-CH_3$		0.666	0.201	3.31	−0.416	−0.03
		0.659	***0.224***	***2.94***	***−0.427***	***−0.02***
−H		0.654	0.243	2.69	−0.417	−0.04
		0.654	***0.256***	***2.55***	***−0.424***	***−0.02***
−*t*-Bu		**0.656**	**0.124**	**5.29**	**−0.419**	**−0.04**
		0.663	*0.150*	*4.42*	*−0.453*	*−0.04*
−*t*-Bu (achiral)		**0.668**	**0.136**	**4.91**	**−0.452**	**−0.04**
		0.671	*0.155*	*4.33*	*−0.455*	*−0.04*
$-NH_2$		**0.629**	**0.187**	**3.36**	**−0.417**	**−0.04**
		0.620	*0.147*	*4.22*	*−0.356*	*−0.04*
***β*CN**		0.640	0.270	2.37	−0.433	−0.04
		0.645	***0.259***	***2.49***	***−0.426***	***−0.02***
3		**0.649**	**0.230**	**2.82**	**−0.397**	**−0.04**
		0.645	*0.259*	*2.49*	*−0.396*	*−0.04*

[a]All values are in numbers of electrons. *q*(*r*) is repulsive polarization, *q*(*s*) is the residual term. Data for the *S*-diastereomers are italicized, and bold indicates the more stable diastereomer. All structures are analyzed at the B3LYP/LANL2DZ level.

further enhance overlap. When the double bond is sterically prevented from achieving the above-plane configuration, back-donation will occur from the lower energy d_{xz} or d_{yz} orbitals, slightly decreasing the stabilization energy. These arguments agree with those made by Hoffmann and co-workers in their theoretical work on the bonding of substituted ethylenes to metals.[48,49]

The VB perspective on the substrate−catalyst interaction emphasizes the resonance between two 16-electron configurations: one corresponding to a simple Lewis donor−acceptor interaction with the alkene π-electrons acting as donor and the metal as an acceptor and the other corresponding to a metallocyclopropane configuration (Figure 13). As we previously have shown, the idealized geometry of the 16-electron metallocyclopropane configuration is a monovacant octahedron (or

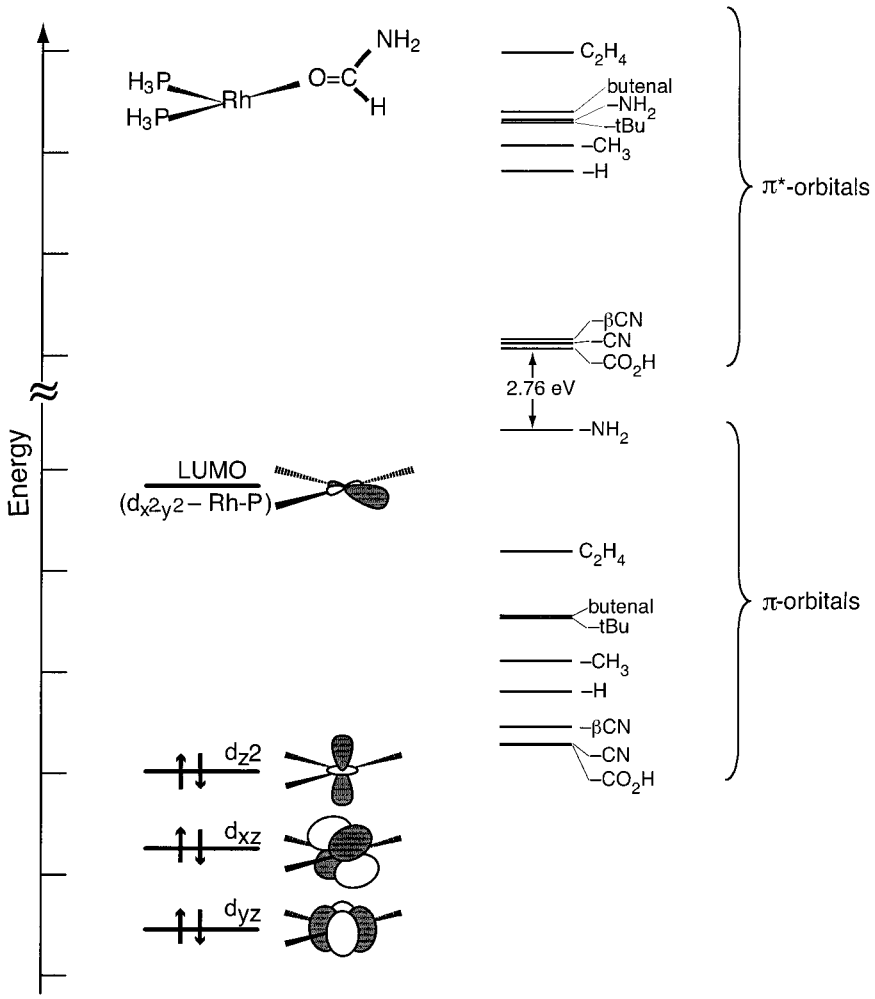

Figure 13. Canonical molecular orbital energy levels for $[Rh(PH_3)_2(formamide)]^+$, showing the filled and unfilled orbitals with the proper symmetry to interact with C=C π and π^* orbitals, seen for the more stable diastereomers and free ethylene on the right. Scale markings are in eV. All calculations were done at the B3LYP/LANL2DZ level.

Scheme 3

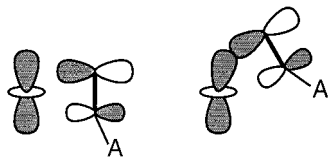

square pyramid with 90° bond angle between axial and basal bonds).[50] Therefore, mixing of metallocyclopropane character with the square-planar donor−acceptor will tend to move the midpoint of the alkene out of the square plane. Whereas the axial Rh−C bond of the metallocyclopropane conforms to a standard two-center−two-electron bond, the bonds of the basal plane are dominated by three-center−four-electron interactions among *trans* ligand pairs. Such interactions create substantial charge accumulation on the basal ligands. When the alkene has an electron-withdrawing substituent, maximum stabilization occurs with that C placed close to the basal plane. For electron-donating substituents, the situation is reversed.

(48) Albright, T. A.; Hoffmann, R.; Thibeault, J. C.; Thorn, D. L. *J. Am. Chem. Soc.* **1979**, *101*, 3801−3812.
(49) Eisenstein, O.; Hoffmann, R. *J. Am. Chem. Soc.* **1981**, *103*, 4308−4320.
(50) Firman, T. K.; Landis, C. R. *J. Am. Chem. Soc.* **1998**, *120*, 12650−12656.

Discussion

One goal of this work is to test current computational methods against empirical data for a fine process: the control of enantioselectivity in enamide hydrogenation. Our results clearly show that modern computations are able to reproduce the enantioreversal that is seen experimentally as the enamide α-substituent is changed from an electron-withdrawing nitrile or carboxylic acid to a bulky *t*-Bu group. In addition, computations agree with experiment in suggesting that hydrogenation of **2** should be substantially slower than **1** ($\Delta\Delta G^{\ddagger}$(**2**−**1**) ≈ 3.5 kcal/mol assuming complete saturation of alkene binding) but should yield very high enantioselectivity ($\Delta\Delta G^{\ddagger}$(**2R**−**2S**) ≈ 6 kcal/mol). Experimentally it has been observed by Gridnev and Imamoto that addition of HD to substrates like **1** leads to preferential addition of D at C_α, whereas addition of HD to enamides similar to **2** shows accumulation of D at C_β.[17,44] Migratory insertion of the alkene into a Rh−H(D) bond controls the D distribution in the product: D inserts more slowly than H. In correspondence with these data, our computations demonstrate a clear preference for the formation of α-alkyl hydrides for **1** but β-alkyl hydrides for **2**.

Despite the success of these computations in reproducing empirical data, one must be cautious in accepting the computed potential energy surfaces too literally.

Ubiquitous issues such as the relevance of gas-phase models to a solution process, computational accuracy limitations, and limitations in conformer searching certainly apply here. To counter these concerns we have chosen systems that are relatively rigid and insensitive to solvent polarity. Also we have applied computational methods that we previously have tested against a large number of empirical data.

Limitations that are more specific to these catalyst systems include the possibility (1) that a "dihydride pathway" may contribute to product formation, (2) that diastereomeric pathways are interconnected by low barrier isomerizations, and (3) that solvent may modulate feasibility of the previous two limitations. Gridnev and Imamoto have compellingly shown that dihydride complexes with the general formula [Rh(diphosphine)(H)(H)(solvent)(solvent)]$^+$ form in methanol solutions at atmospheric pressure and low temperatures when the diphosphine is electron rich.[44] They have also demonstrated that such complexes react rapidly with enamides to yield alkyl hydride complexes and, ultimately, hydrogenated product. These results raise the possibility that catalytic hydrogenation with electron-rich diphosphines may proceed via a "hydride route", for which formation of a dihydride precedes enamide association, rather than an "olefin route". In principle, one can compute energies for the dihydride routes as well, but such computations are time-consuming and complicated by the intimate role, and many possible trajectories, of solvent association and dissociation in the reaction process. Similarly, there are many possible routes for isomerization between diastereomeric pathways. As we have shown previously, the most plausible paths involve alkene dissociation, which is likely to involve solvent participation as well. Although such computational explorations are possible, at this time it is unclear whether enough insight can be gained to justify the effort.

For the specific case of the hydrogenation of **2**, it is interesting to consider whether critical features, such as the enantioreversal relative to **1**, would result if the dihydride route or interpathway isomerization was important. If all dihydride isomers shown in Figure 7 were in rapid equilibrium, either because they formed via the dihydride route or because they isomerized, the insertion of alkene into a Rh−H bond would most likely be turnover-limiting and enantiodetermining. As Figure 7 shows, the dominant hydrogenation pathway would give the *S* product isomer via a β-alkyl hydride intermediate. Thus, correspondence between modeling and the empirical observations of enantioreversal and D accumulation at C_β is retained.

This computational study provides insight into the α-substituent effect in enamide hydrogenation. This effect has been well-documented, but poorly understood. Recent experimental results of Gridnev and Imamoto[17] and the computational results reported herein converge in the sense that both models emphasize the relative stabilities of α- and β-alkyl hydrides as the α-substituent is changed. Not only is it satisfying that two very different approaches yield similar explanations, but these efforts illustrate nicely how modern computations and experiment can address a problem independently, on similar time scales, and in complementary fashions. Overall the α-substituent effect can be traced to shifting of the C═C out of the square plane in a direction that is controlled by the electron-withdrawing vs electron-donating character of the α-substituent. Electron-withdrawing groups lead to a strong preference for C_α to lie in the square plane, thus displacing C_β out of plane. It is the proximity of this group with the Me-DuPHOS methyl groups that determines which enantioface binds more tightly. The less stable diastereomer must distort to alleviate the steric interaction between C_β and Me-DuPHOS; although there is an energetic penalty for this distortion, it pushes the substrate along the reaction pathway that leads to H_2 addition and the more stable α-alkyl hydride. In contrast, the more stable diastereomer is predisposed to add H_2 in a way that would yield the slower forming and less stable β-alkyl hydride. Each of these arguments is reversed when the α-substituent is a bulky electron-donating group such as *t*-Bu. An interesting prediction of this analysis is that when HD is the reductant, the less abundant product could have D accumulate in the opposite site relative to the more abundant product.

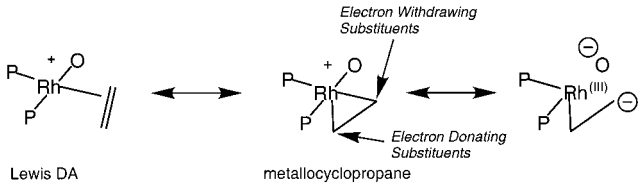

Figure 14. Alternative valence bond pictures of the catalyst−enamide adduct. Only one of the four three-center−four-electron resonance structures is shown (far right). Electron-withdrawing substituents prefer the basal position of the square pyramidal metallocyclopropane structure, while electron-donating substituents prefer the axial position.

The demonstration that computation faithfully reproduces experiment and leads to insight suggests that computation is a valuable tool to be used in concert with experiment. We are now turning to the use of computations to help guide the design of new ligands for asymmetric catalysis and to interpret empirical mechanistic data.

Acknowledgment. We thank the NSF for financial support and the National Center for Supercomputer Applications for computational time on the SGI CRAY ORIGIN200 computer system under CHE970025N. We gratefully acknowledge Professor John Brown's kind sharing of information prior to publication, and helpful correspondence with Professors Imamoto and Gridnev.

Supporting Information Available: Gaussian 98 code changes, figures for structures along the **R-C** and **S-A** pathway, tables of NBO analysis results, and Cartesian coordinates and total energies for all structures. This material is available free of charge via the Internet at http://pubs.acs.org.

OM010060T